




Please cite the Published Version

Ghanbariha, M , Farvizi, M , Ataie, SA, Alizadeh Samiyan, A, Liskiewicz, T  and Kim, HS (2024) Effect of YSZ Particle Size and Content on Microstructure, Mechanical and Tribological Properties of (CoCrFeNiAl)_{1-x}(YSZ)_x High Entropy Alloy Composites. *Metals and Materials International*, 30 (9). pp. 2523-2539. ISSN 1598-9623

DOI: <https://doi.org/10.1007/s12540-024-01656-2>

Publisher: Springer

Version: Accepted Version

Downloaded from: <https://e-space.mmu.ac.uk/634462/>

Usage rights:  In Copyright

Additional Information: This version of the article has been accepted for publication, after peer review and is subject to Springer Nature's AM terms of use (<https://www.springernature.com/gp/open-research/policies/accepted-manuscript-terms>), but is not the Version of Record and does not reflect post-acceptance improvements, or any corrections. The Version of Record is available online at: <http://dx.doi.org/10.1007/s12540-024-01656-2>

Enquiries:

If you have questions about this document, contact openresearch@mmu.ac.uk. Please include the URL of the record in e-space. If you believe that your, or a third party's rights have been compromised through this document please see our Take Down policy (available from <https://www.mmu.ac.uk/library/using-the-library/policies-and-guidelines>)

1 **Effect of YSZ Particle Size and Content on Microstructure, Mechanical and**
2 **Tribological Properties of (CoCrFeNiAl)_{1-x}(YSZ)_x High Entropy Alloy Composites**

3

4 **M. Ghanbariha ^a, M. Farvizi ^{a,*}, S.A. Ataie ^{b,*}, A. Alizadeh Samiyan ^a,**
5 **T. Liskiewicz ^c, H.S. Kim ^{d,e}**

6

7 ^a *Department of Ceramic, Materials and Energy Research Center, Karaj, 31787-316, Iran*

8 ^b *Iran University of Science and Technology, School of Metallurgy and Materials Engineering, Narmak,*
9 *Tehran 16846–13114, Iran*

10 ^c *Department of Engineering, Faculty of Science and Engineering, Manchester Metropolitan University,*
11 *Manchester M1 5GD, UK*

12 ^d *Graduate Institute of Ferrous and Energy Material Technology, Pohang University of Science and*
13 *Technology, Pohang, 37673, Republic of Korea*

14 ^e *Advanced Institute for Materials Research (WPI-AIMR), Tohoku University, Sendai, 980-8577, Japan*

15

16

17 * Corresponding Author: M. Farvizi

18 Email: mmfarvizi@yahoo.com, mmfarvizi@merc.ac.ir

19 Fax: +98-21-88773352; Tel: +98-935 848 5439

20 ORCID ID: <https://orcid.org/0000-0003-3225-4788>

21

22

23 **Abstract**

24 High entropy alloy composites (HEACs) have recently been explored for use in industrial applications. This
25 study investigates the impact of particle size (micro or nano) and content (5 and 10 wt.%) of YSZ on the
26 microstructure and tribological properties of AlCoCrFeNi. The samples were prepared using a
27 combination of mechanical alloying and spark plasma sintering. XRD results and Rietveld analysis reveal
28 that HEACs with micro-sized YSZ have a higher BCC/FCC ratio. FESEM and EDS results confirmed the
29 evolution of Al-rich regions in the vicinity of the reinforcements. Especially, in HEA-10NanoYSZ-
30 sample, due to higher interfacial regions, a huge amount of Al-rich phase has been formed which yields
31 the reduction of BCC phase content in this sample. Microhardness and pin-on-disc wear tests show that
32 the samples reinforced with microparticles demonstrate better performance compared to nanocomposite
33 samples. For example, HEA-10MicroYSZ-sample exhibits the highest hardness (5.1 GPa) and the lowest
34 wear characteristics (with a coefficient of friction of 0.8 and a wear rate of $4 \times 10^{-4} \text{ mm}^3/\text{N.m}$). This can be
35 correlated to the higher hardness and BCC phase content, and grain boundary strengthening in the
36 microcomposites.

37 **Keywords:** High entropy alloy composites; Micro/nano YSZ particles; Microstructure; Hardness; Wear.

38

39 **1. Introduction**

40 Before the year 2004, industrial metallic parts were typically produced using binary or ternary alloys.
41 However, a new class of materials called high entropy alloys (HEAs) emerged after this period [1-3].
42 HEAs are created by combining multiple elements using various production methods. HEAs can be
43 produced by melting and casting, additive manufacturing, mechanical alloying, spark plasma sintering
44 (SPS), and deposition techniques [4-9]. HEAs have gained considerable attention in a wide range of
45 industries and advanced multi-functional applications. They find applications in diverse fields such as
46 medical parts [10], molds and marine structures [11], electrodes for water electrolysis [12], mechanical
47 components, aerospace, and high-temperature parts [13]. HEAs are characterized by the presence of at
48 least five metallic elements and can be broadly classified into two categories: equimolar and non-
49 equimolar types. Each constituent element should have an atomic percentage of at least 5% to meet the
50 condition for entropy, which is required to be at least $1.5R$ (where R represents the gas constant). These
51 multi-element alloys exhibit significant improvements in their physical and mechanical properties. These
52 advancements can be attributed to the unique microstructure of HEAs, which is a result of the high content
53 of different metals present. The presence of multiple elements contributes to sluggish diffusion, severe
54 lattice distortion, and the cocktail effect. These distinctive features ultimately lead to enhanced hardness,
55 yield strength, ductility, oxidation resistance, and thermal stability [14, 15].

56 While a wide range of metallic elements can be utilized in the production of HEAs, transition metals are
57 commonly employed. Fe, Cr, Co, and Ni are easily dissolved due to the atom substitution rules, which
58 take into account factors like enthalpy of mixing, electronegativity, and atomic size. Therefore, the typical
59 composition of an HEA system consists of FeCoCrNi+M, where M represents elements such as Al, Ti,
60 Mn, or Cu [9, 16-20]. Al plays a vital role as the major alloying element in most HEAs, primarily due to
61 its stabilizing effect on both FCC and BCC phases. Consequently, the AlCoCrFeNi system has been
62 extensively studied in numerous research papers and the optimum content of each element is nearly
63 investigated to have higher mechanical properties [21-26]. Each property of HEAs is highly affected by
64 the microstructure, which is influenced by several key factors, including grain size, shape and distribution
65 of secondary phases, as well as the presence of dislocations and twinning. It is worth noting that the
66 microstructure in this system typically consists of a solid solution with one or two phases. Therefore, the
67 ratio of FCC to BCC phases is of utmost importance, as it can significantly impact the physical and
68 mechanical properties of the HEA. Generally, BCC HEAs tend to exhibit high strength, while FCC
69 structures often demonstrate enhanced fracture strain and toughness [27, 28]. However, it should be noted

70 that high entropy alloys (which predominantly consist of metallic elements) often exhibit limited load-
71 bearing capacity and possess moderate hardness and wear resistance. Therefore, there is a need to
72 introduce an enhanced system to address these limitations.

73 The incorporation of a reinforcement phase has been proven to significantly enhance the hardness and
74 tribological properties of HEAs, particularly through the introduction of ceramic particles. This novel
75 system, known as metal matrix composites (MMCs [29]), involves combining HEAs with carbides (such
76 as WC, TiC [30, 31]), nitrides (such as TiN [32]), or oxides (such as ZrO₂, Al₂O₃ and Y₂O₃ [33-35]). The
77 addition of ceramic particles has the potential to augment mechanical properties through two primary
78 mechanisms: reduction of the average grain size and hindrance of dislocation movement, attributable to
79 the strengthening effect at the grain boundaries [31-36]. In the case of high entropy alloy composites
80 (HEACs), which consist of dissimilar materials (metals and ceramics), it is crucial to have two materials
81 with compatible physical properties. This compatibility is essential in order to minimize the undesired
82 effects of mismatch and distortion. Hence, oxides are typically the preferred choice among various ceramic
83 particles. In general, this preference arises from their inherent advantages, including better chemical
84 stability and adhesion to the parent phase (they have coefficient of thermal expansion values near HEAs)
85 [37]. Moreover, oxides usually show lower friction coefficients and wear rates (which can be attributed to
86 their lower shear strength) [38]. Hence, the utilization of oxide-dispersion strengthening (ODS) represents
87 a promising approach for augmenting the strength of metallic alloys, particularly HEAs. The addition of
88 micro-sized Y₂O₃, Al₂O₃, and ZrO₂ particles to HEAs has been shown to enhance hardness, compressive
89 yield strength, and reduce wear. In the recent articles [39, 40], the authors specifically examined the impact
90 of incorporating micro-sized ZrO₂ particles into the AlCoCrFeNi alloy. Several studies [33, 34, 41] have
91 examined the impact of incorporating nano-sized ZrO₂, Al₂O₃, and Y₂O₃ on the mechanical properties of
92 HEAs. However, due to the presence of multiple strengthening mechanisms in ODS-HEACs (such as
93 grain boundary strengthening, the Hall-Petch mechanism, solid solution strengthening, and Orowan
94 strengthening [42, 43]) the size and content of reinforcement particles present a complex challenge. This
95 is because the mechanical responses can be significantly altered by the same oxide particle with different
96 sizes or content.

97 Among various oxides, Yttria Stabilized Zirconia (YSZ) is the preferred choice due to its unique
98 properties. The primary advantage of utilizing YSZ lies in its stability and robust thermal shock resistance.
99 Because during the heat treatment of zirconia, a transformation occurs from the tetragonal to monoclinic
100 phases. This transformation is accompanied by a 3-4 vol% expansion, which can have a detrimental impact

101 on the performance of composites. To address this issue, the addition of Y_2O_3 dopant can stabilize the
102 tetragonal phase of zirconia, resulting in what is known as Yttria Stabilized Zirconia [44]. In addition,
103 YSZ represents a high thermal expansion coefficient which plays a crucial role in ensuring interface
104 compatibility between oxide particles and the metal matrix [45]. Moreover, first-principles calculations
105 [46] have demonstrated that the addition of yttria to zirconia can lead to increased hardness and decreased
106 elastic modulus. Therefore, based on the theory that fracture toughness is directly proportional to the H/E
107 ratio [47, 48], it can be inferred that the addition of yttria can improve fracture toughness. It was verified
108 that YSZ exhibits high compressive strength and under mechanical loading, YSZ undergoes a stress-
109 induced transformation that serves to augment its fracture toughness [49]. Also, another piece of evidence
110 from Raja et al. [50] confirms that YSZ has higher fracture toughness compared to both zirconia and
111 zirconia-toughened alumina. However, investigations into the effects of adding YSZ particles on
112 microstructure and mechanical properties are relatively scarce in the literature. The previous literature
113 primarily focuses on examining the impact of incorporating ZrO_2 , Al_2O_3 , and Y_2O_3 (rather than YSZ) into
114 HEAs on their mechanical properties. Furthermore, comprehensive surface characteristics (encompassing
115 hardness, wear properties such as friction coefficient and wear rate, and phase structure through Raman
116 analysis simultaneously) of analogous ODS-HEACs have not yet been documented.

117 The primary aim of this paper is to investigate the influences of YSZ size (nano or micro) and content (5
118 wt% or 10 wt%) on the morphology and phase structure of AlCoCrFeNi high-entropy alloys (with XRD,
119 SEM/EDS, and Raman spectroscopy techniques). To fabricate these ODS-HEAC samples, a combination
120 of mechanical alloying and spark plasma sintering techniques is employed. Consequently, a
121 comprehensive analysis of the hardness and wear characteristics of the HEA composites will be conducted
122 through indentation and sliding tests. Finally, a discussion will be presented to elucidate the relationships
123 between the microstructure and mechanical properties of the materials. As YSZ levels were selected
124 identically (5 and 10 wt%), the comparison between composites with nano-sized particles and those with
125 micro-sized particles allows for a better understanding of the effects of particle size on the microstructure
126 and performance of the HEAs. This comparison can provide valuable insights into the potential advantages
127 and limitations of using nano-sized particles in composite materials.

128

129

130

131 **2. Materials and methods**

132 **2.1. Sample production**

133 Micro-sized metal particles (particle size was lower than 45 μm) with a purity degree exceeding 99% were
134 utilized as the initial materials. These metal particles included aluminum (manufactured by Xinji
135 Guangyuan), Co-Cr-Fe (produced by Merck), and nickel (obtained from Aldrich). Additionally, micro-
136 sized YSZ ($\text{ZrO}_2\text{-8 wt\%Y}_2\text{O}_3 \sim 15 \mu\text{m}$) and nano-sized YSZ (40-60 nm, Aldrich) were employed as
137 ceramic reinforcements. The powders exhibited a spherical shape. The aforementioned powders
138 underwent mechanical alloying followed by sintering using the SPS technique. A schematic of the
139 combinational procedure is depicted in Figure 1. Additionally, for a detailed perspective, temperature-
140 displacement curves of the samples using the SPS method are illustrated in Figure 2. For this particular
141 study, a total of five samples were prepared, each differing in terms of the YSZ size and content.
142 Additional information and supporting data are available in references [40].

143

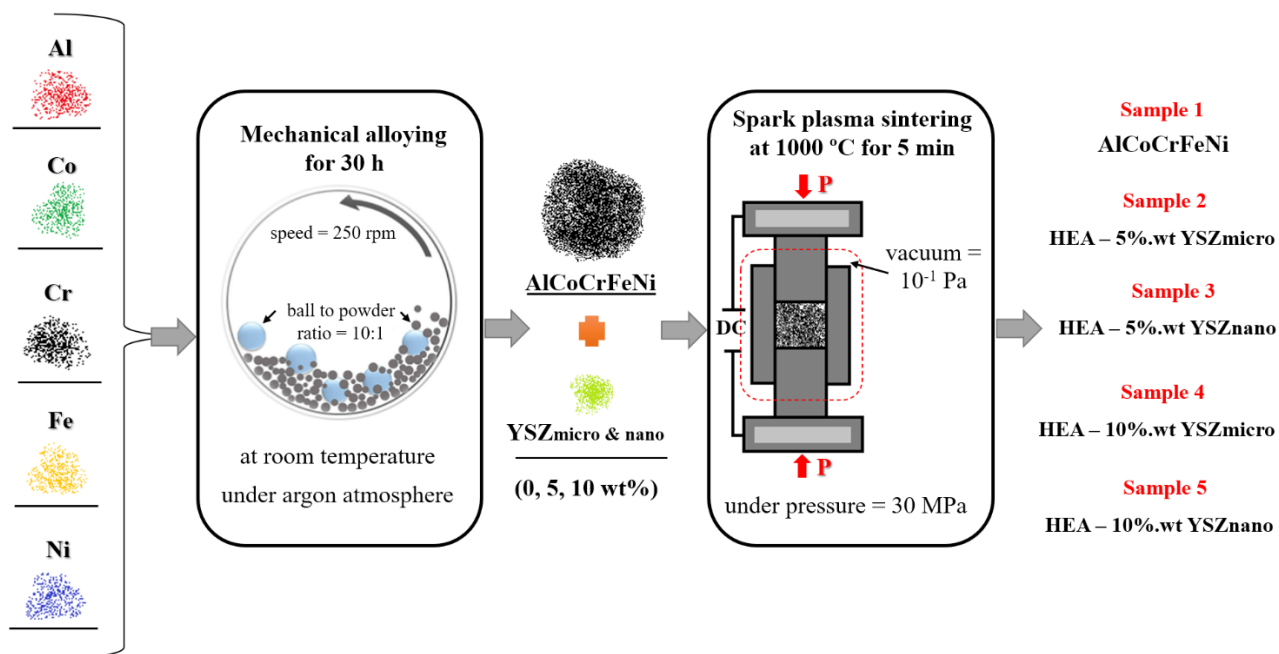


Fig. 1: MA and SPS production schematic.

144

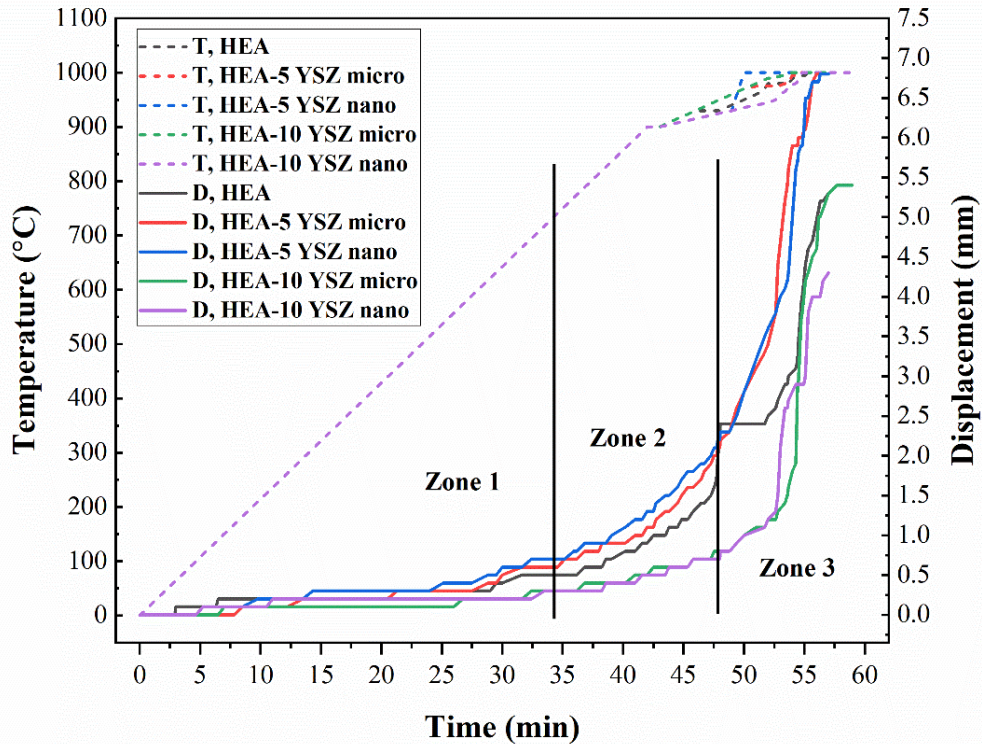


Fig. 2: Variation of SPS temperature and punch displacement against sintering time during the SPS process of HEA-YSZ composites.

145

146 2.2.Characterization methods

147 X-ray diffraction (XRD) analysis was conducted using a Siemens-Germany D-500 instrument, operating
 148 with Cu K α radiation ($\lambda = 1.54 \text{ \AA}$), to perform phase analysis. Furthermore, the phase contents of the
 149 samples were determined through Rietveld refinement analysis, employing MAUD software. The
 150 morphology and elemental analysis of the samples were evaluated using scanning electron microscopy
 151 (SEM) equipped with energy-dispersive spectroscopy (EDS). The SEM-EDS analysis was carried out
 152 using a TESCAN MIRA3 instrument from Czech Republic. In addition, Raman spectroscopy (Uni-
 153 DRON, South Korea) was employed to investigate the bond structure of each sample, both before and
 154 after the sliding test. An Ar-ion laser with midrange Rayleigh wavelength (532 nm) was utilized, and the
 155 resolution was set at 1 cm^{-1} . It is important to note that prior to the analysis of Raman spectra, it is
 156 advisable to remove any noise and apply baseline correction.

157 To mitigate the roughness effect, the surface of the samples was polished using a diamond probe with a
 158 contact load of 0.1 mN prior to conducting mechanical tests. Subsequently, the surfaces were cleaned

159 using cotton swabs. Microhardness measurements were performed utilizing the Vickers microhardness
160 indenter (FM-600, Future-Tech Corp, Japan). To ensure accuracy and reliability, multiple measurements
161 were taken for each sample from distinct regions, with a minimum of five repetitions.

162 The pin-on-disc wear machine (Abrasion Tester) available at Iran University of Science and Technology
163 was utilized to evaluate the wear characteristics of the samples. The tests were conducted under ambient
164 conditions, specifically at room temperature with a humidity level of 30%. The sliding was performed
165 without the application of any lubrication. The counter pin used was a tungsten carbide ball with a diameter
166 of 5 mm. The test parameters were set as follows: a fixed load of 30 N and a sliding speed of 0.07 m/s.
167 The sliding distance for all the samples was standardized at 200 m. Each sample underwent three
168 repetitions of the pin-on-disc test, and the average data for the friction coefficient and wear rate were
169 recorded. It is important to note that the wear rate for each sample was calculated using the formula $k =$
170 $V / (S \cdot F)$, where V shows the volume of mass loss, S represents the sliding distance, and F denotes the
171 constant load.

172

173 **3. Results and discussion**

174 **3.1. Microstructure**

175 The equiatomic HEA powder (after mechanical alloying) exhibits a BCC phase (Fig. 3a) due to the
176 prevalence of BCC state in most of its constituent elements such as Fe, Cr, Co, and Al, whether occurring
177 naturally (as in the case of Fe and Cr) or induced artificially (as high stresses during ball milling can lead
178 to the manifestation of BCC structure in Co and Al elements). Following the heating process (SPS
179 process), the unreinforced HEA sample undergoes a significant increase in the FCC phase (Fig. 3b), as
180 the BCC to FCC transformation of this alloy takes place at approximately 650 °C [51, 52]. The XRD
181 patterns of the HEAC samples, as shown in Figs. 3c-3f, reveal some important features of the
182 microstructure. Firstly, three phases (FCC, BCC, and oxide) are presented in the AlCoCrFeNi-YSZ
183 composites at the same time. Secondly, the BCC peaks at 64.7° and 82.2° are absent in the last sample
184 (HEA-10YSZ nano). Thirdly, the YSZ peak at 59° is absent in the nano-sized samples. In addition, the
185 intensity of BCC peak at 44° decreases as the YSZ content increases and the YSZ size decreases. Since
186 the BCC and FCC peaks overlap in the samples, the high-resolution XRD patterns in the range of 42° to
187 52° have been represented in Fig. 4. Furthermore, by performing Rietveld refinement analysis, the phase
188 percentages for each sample are calculated and shown in Fig. 5. The results indicate that the BCC to FCC

189 phase fraction is high in micro-sized ODS-HEACs (HEA-5YSZmicro and HEA-10YSZmicro), whereas
190 this ratio is low in nano-sized ODS-HEACs, particularly in HEA-10YSZnano. Further, at the same oxide
191 particle size, this ratio diminishes with an increase in YSZ content. Fig. 6 demonstrates the clear presence
192 of oxide bonds in the HEAC samples. While metallic samples typically do not exhibit Raman peaks [12,
193 25], the first sample (HEA) displays a few minor peaks associated with the minor content of oxides (AlO_x ,
194 FeO_x , and CrO_x phases) present in the sample. Upon the addition of YSZ particles in HEACs, there is an
195 observed increase in the number of peaks and the height/intensity of the peaks. The broad peaks detected
196 at 494 cm^{-1} , 510 cm^{-1} , 630 cm^{-1} , 671 cm^{-1} , 1010 cm^{-1} , 1398 cm^{-1} , and 1590 cm^{-1} are attributed to YSZ,
197 Al_2O_3 , YSZ, Cr_2O_3 , Fe_2O_3 , Fe_2O_3 and Cr_2O_3 , respectively. This phenomenon is anticipated as it suggests
198 an interaction of oxide bonds at different frequencies. Our analysis of peak locations closely aligns with
199 that of other references [25, 53-57], exhibiting a high degree of concordance.

200 To understand the observed phase evolution in the prepared samples, SEM micrographs at different
201 magnifications are presented in Fig. 7(a-e). In this figure, FCC, BCC, Al-rich, and reinforcement/YSZ
202 phases are illustrated with arrows. It can be inferred that the grain size is larger in micro-sized ODS-
203 HEACs. However, it is evident that YSZ particles are well dispersed in the micro-sized samples, while
204 the dispersion of YSZ is not as effective in the nano-sized samples. Additionally, the elemental
205 contribution of BCC and FCC phases is presented in Table 1. Based on the EDS elemental percentages, it
206 is important to highlight that the composition of the BCC phase is rich in Ni and Al, while the FCC phase
207 contrasts with a richness in Fe and Cr. The distribution of cobalt element is almost similar in both of FCC
208 and BCC phases. Furthermore, the FCC phase fraction increases with the higher content of YSZ particles
209 and reinforcement particle size reduction, which aligns well with the XRD-Rietveld analysis results.
210 Among Al-Co-Cr-Fe-Ni elements, aluminum has the highest diffusion coefficient at the sintering
211 temperature. Therefore, in the matrix-reinforcement interfaces, this element diffused out from Ni-Al-rich
212 BCC phase toward interfacial regions. This leads to the evolution of the Al-rich zone in the microstructure
213 and the reduction of BCC phase fraction in the composite samples. It should be noted that in the samples
214 reinforced with nanometric YSZ particles which contain higher interfaces, the formation of the Al-rich
215 phase is more pronounced. Therefore, the black regions at the interfaces consist of an Al-rich phase.
216 However, due to the SPS process, other dispersed black areas (with low content) can be attributed to the
217 presence of pores.

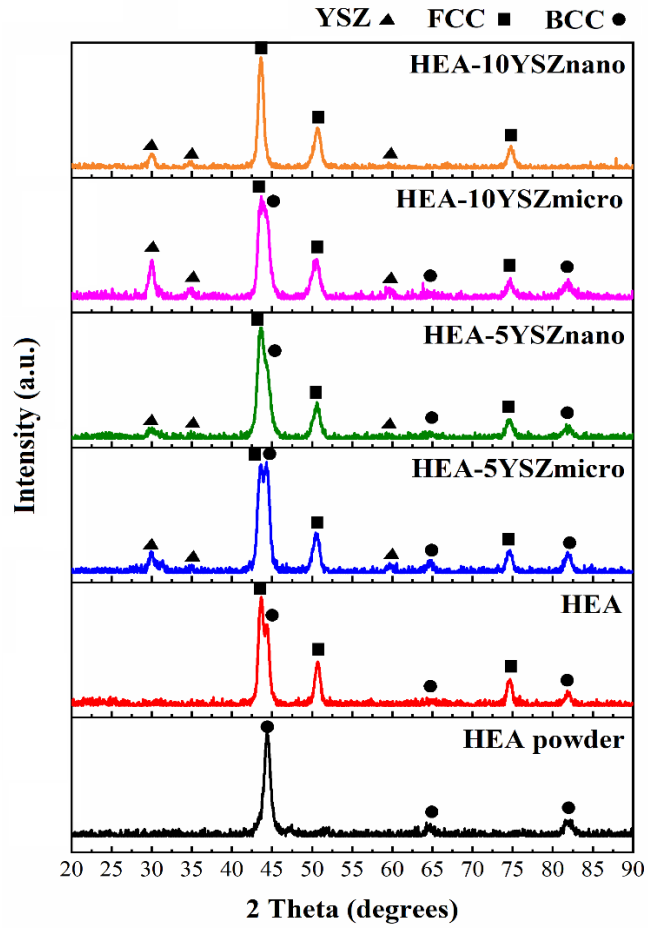
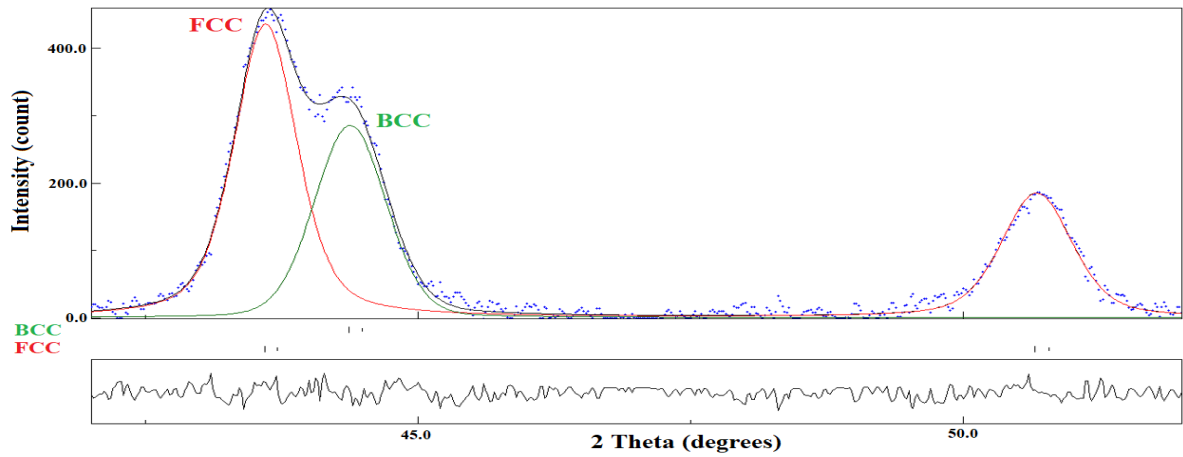


Fig. 3: XRD analysis for (a) HEA powder [39], (b) HEA [39], (c) HEA-5 wt% YSZmicro, (d) HEA-5 wt% YSZnano, (e) HEA-10 wt% YSZmicro, and (f) HEA-10 wt% YSZnano samples.

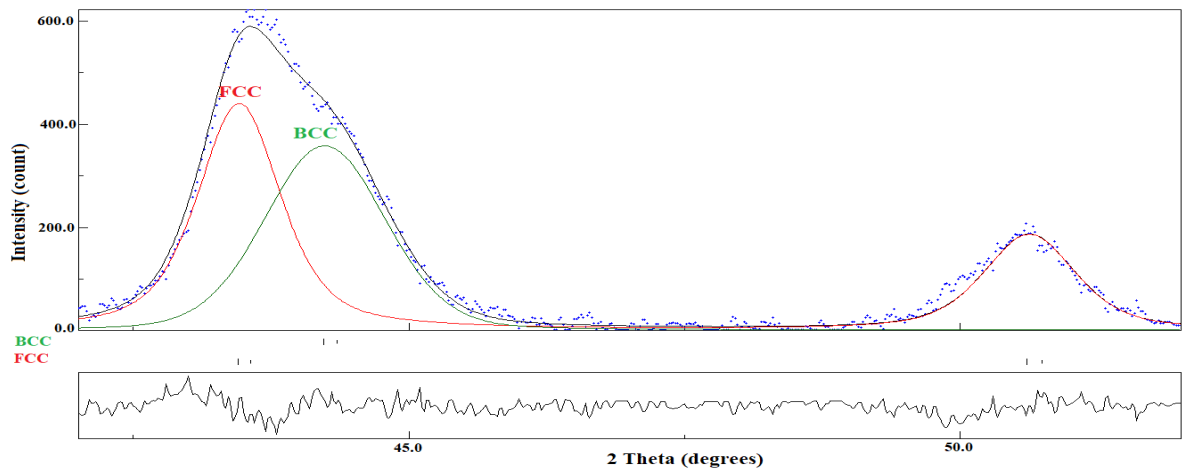
218

219

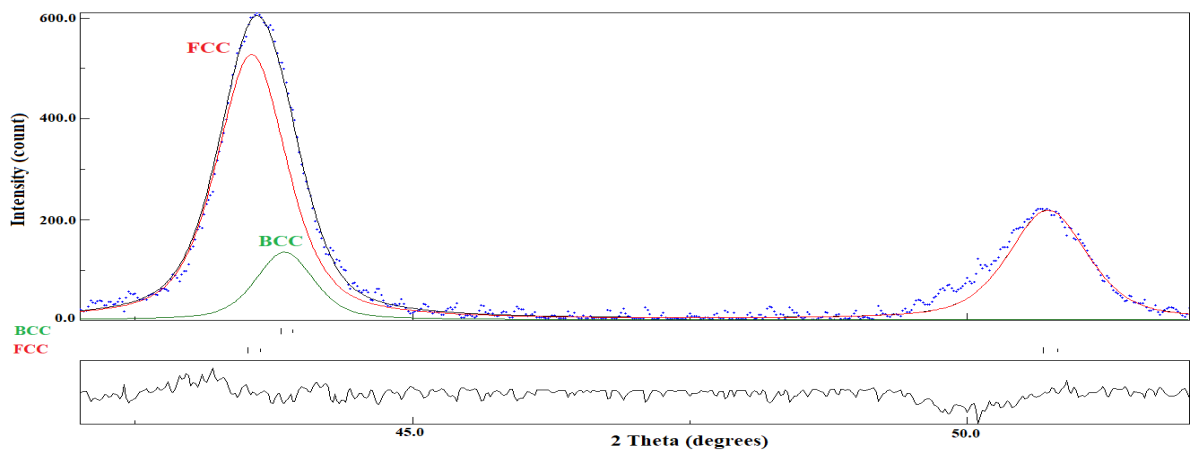
220



(a)

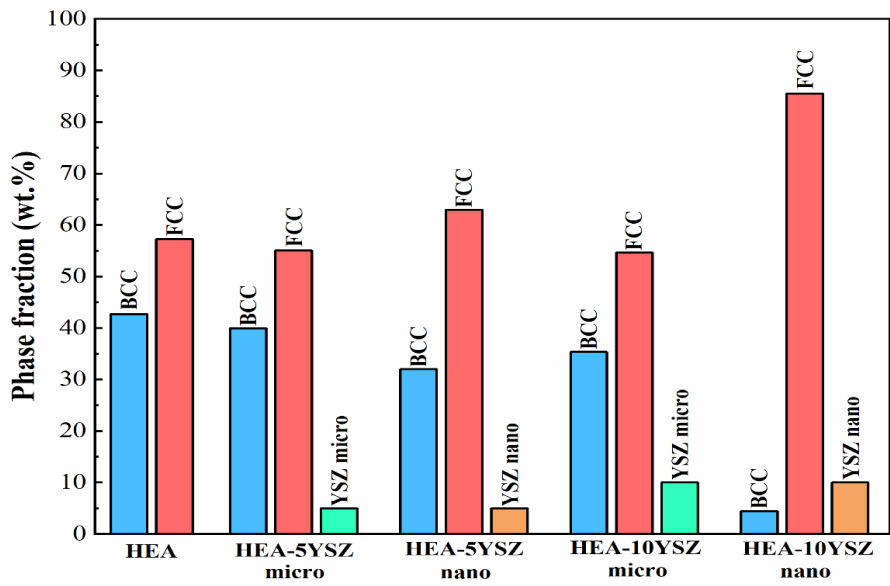


(b)



(c)

Fig. 4: Detailed scans for FCC and BCC phases; (a) HEA [39], (b) HEA+ 5wt% YSZnano, and (c) HEA+ 10 wt% YSZnano samples.



221

Fig. 5: Phase fraction of HEA-YSZmicro and HEA-YSZnano samples obtained from Rietveld refinement analysis.

222

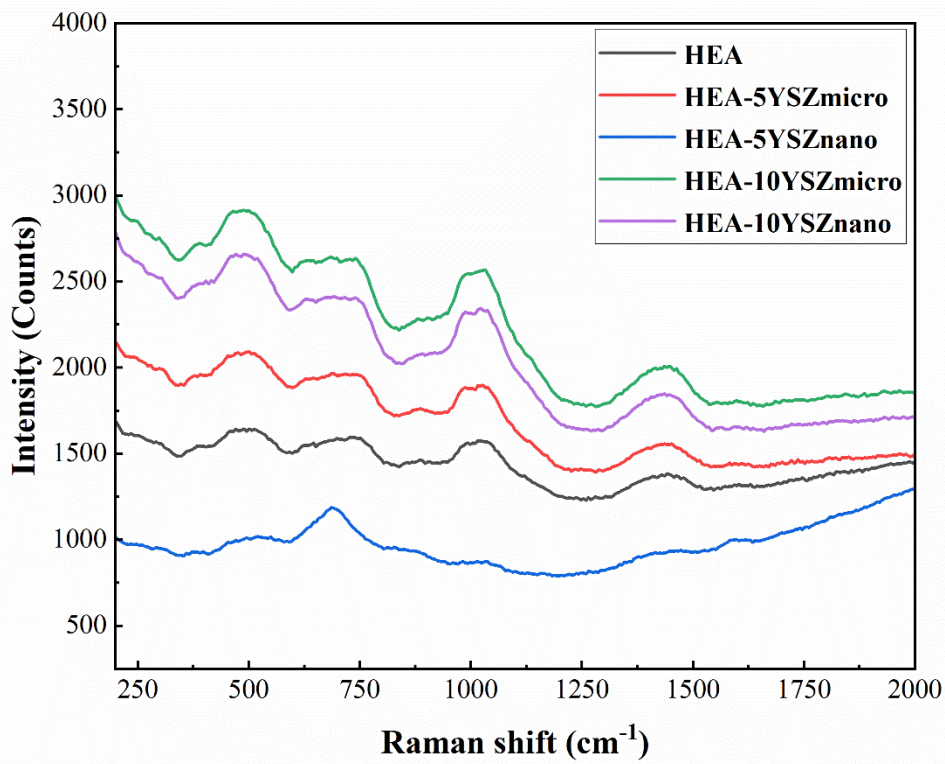
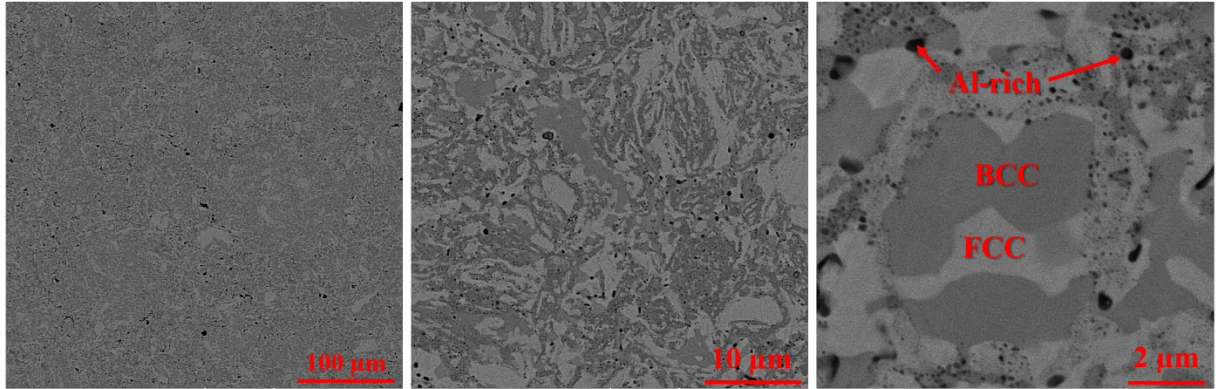
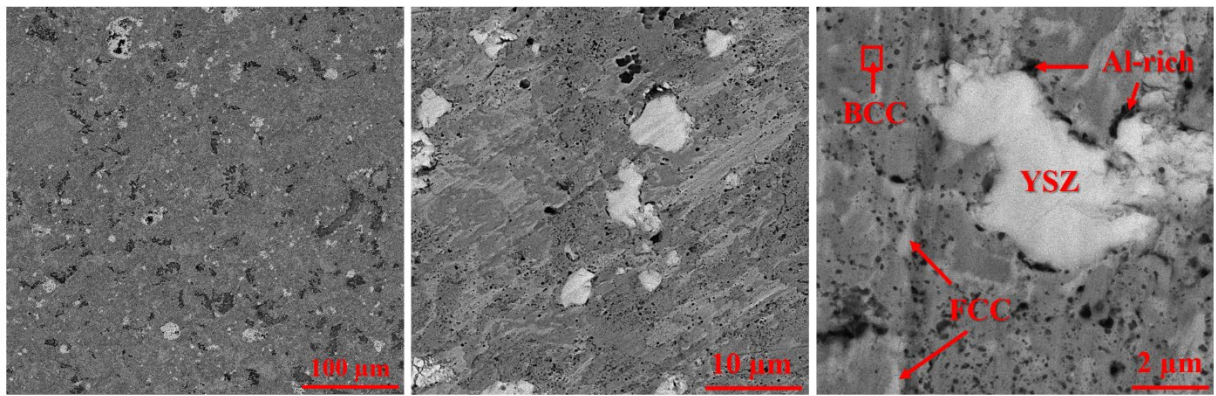


Fig. 6: Raman spectra of samples.

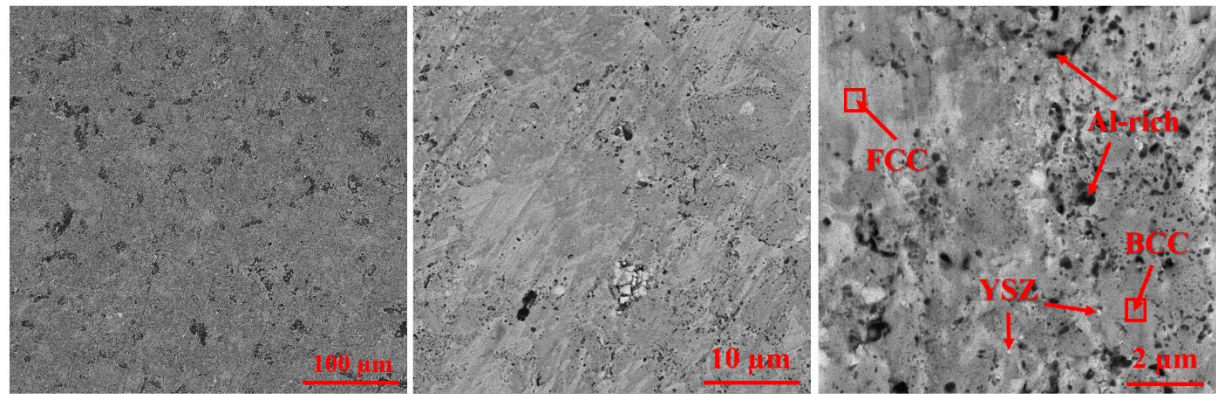
223



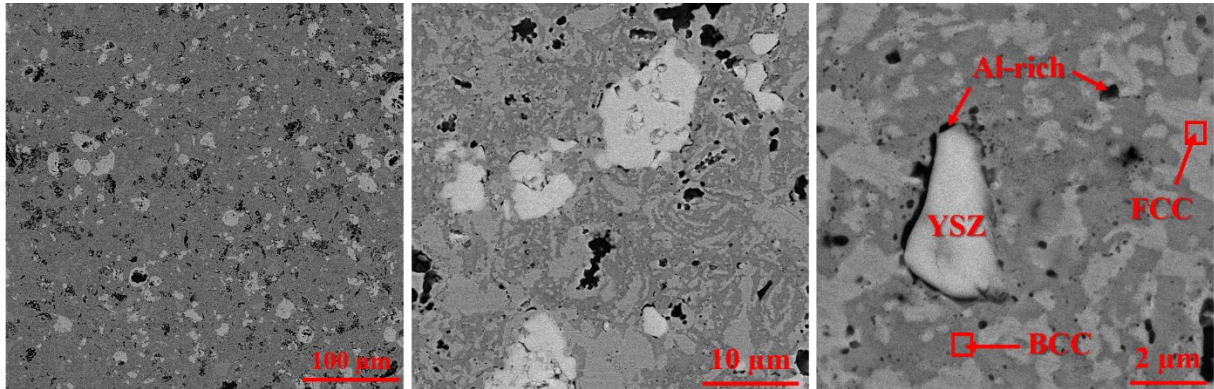
(a)



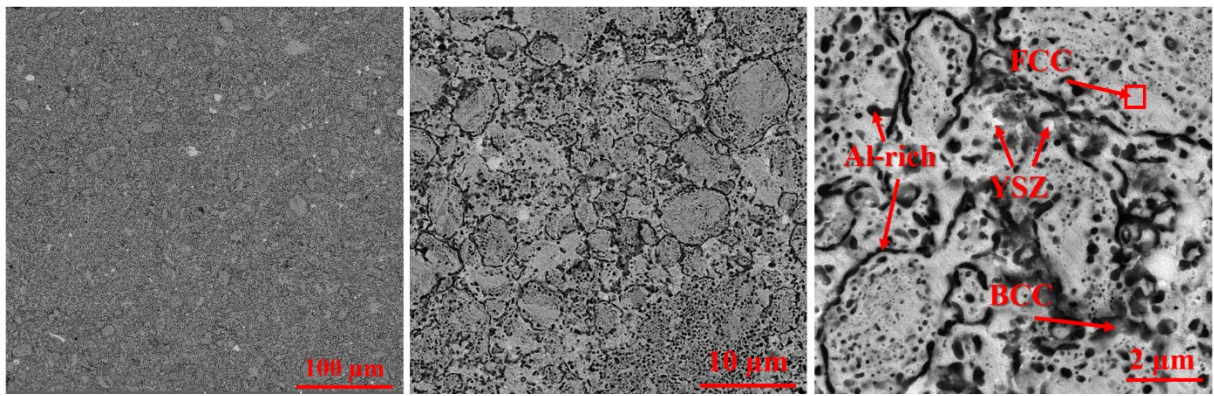
(b)



(c)



(d)



(e)

Fig. 7: SEM and FESEM images of (a) AlCoCrFeNi, (b) HEA-5wt% YSZmicro, (c) HEA-5wt% YSZnano, (d) HEA-10wt% YSZmicro, and (e) HEA-10wt% YSZnano.

224

225

226

227

228

229

230

231

232

Table 1: EDS analysis results deduced from HEA-YSZ in different phases (in wt%).

Sample	Phase	Al	Co	Cr	Fe	Ni
HEA	FCC	5.71	24.88	22.24	28.04	19.13
	BCC	29.45	18.97	14.44	17.42	19.71
HEA-5YSZmicro	FCC	9.22	19.86	26.55	25.23	19.14
	BCC	18.36	17.96	10.35	16.89	32.10
HEA-5YSZnano	FCC	3.74	22.21	25.50	28.74	19.81
	BCC	19.90	19.59	6.76	13.65	40.10
HEA-10YSZmicro	FCC	4.32	26.21	23.45	29.40	16.63
	BCC	17.03	23.81	9.85	17.29	32.02
HEA-10YSZnano	FCC	6.34	24.92	21.64	23.43	23.67
	BCC	11.16	23.30	20.29	21.86	23.39

233

234

3.2. Mechanical properties

235

236

237

238

239

240

241

242

243

244

245

246

247

248

249

250

Fig. 8 illustrates the hardness data of AlCoCrFeNi-YSZ composites obtained from the Vickers hardness test. Several observations can be drawn directly from these data. Firstly, it is evident that oxide particles contribute to an increase in hardness. This finding holds true when comparing the hardness of HEA-10YSZmicro with the hardness of HEAs examined in other studies [4, 24]. Secondly, for the same YSZ size, a higher content of reinforcement leads to greater hardness. This finding aligns with the Vegard law, which posits that an increased presence of ceramic particles (due to their higher hardness and elastic modulus compared to metals) raises the average hardness of MMCs. Importantly, this result is consistent with prior studies [34, 41]. Thirdly, when holding the YSZ content constant, samples with micro-sized oxide particles exhibit higher hardness. This finding is complex and warrants further explanation, as multiple mechanisms come into play that can influence the mechanical properties. On one hand, the Hall-Petch mechanism and the smaller grain size of the nano-sized samples suggest higher hardness for HEA-5YSZnano/HEA-10YSZnano compared to HEA-5YSZmicro/HEA-10YSZmicro. However, on the other hand, factors such as solid solution, grain boundary, and Orowan strengthening mechanisms contradict the former mechanism. One contributing factor is the higher BCC phase fraction in micro-sized YSZ samples (as this phase has higher strength than FCC phases [24, 40]), leading to significant solid solution strengthening in these samples. Additionally, in MMCs with high metallic percentages, inter-type (micro-

251 sized) strengthening prevails over intra-type (nano-sized) strengthening [58], resulting in higher fracture
252 strength of micro-sized samples. This underscores the dominance of grain boundary strengthening in this
253 scenario. Furthermore, due to the common occurrence of agglomeration of nanoparticles, YSZ dispersion
254 is not perfect in nano-sized samples, limiting the dominance of the Orowan strengthening mechanism in
255 these samples, while it can occur effectively in micro-sized samples.

256 Fig. 9 displays the SEM images depicting the worn surfaces of the AlCoCrFeNi-YSZ composites. The
257 wear width and specific wear rate data derived from these images are presented in Fig. 10. A comparison
258 of the wear widths/rates of the HEAC samples and the HEA sample [26] indicates the advantageous
259 influence of oxide dispersion strengthening on the wear characteristics. This result is consistent with
260 findings from previous studies [40, 50]. Furthermore, it is noteworthy that the wear characteristics of the
261 samples with micro-sized YSZ are superior to those with nano-sized YSZ. Additionally, a higher content
262 of oxide particles can result in increased wear resistance. This can be attributed to the elevated hardness
263 level, which can lead to increased wear resistance [21, 47, 48]. For a detailed examination of wear patterns,
264 higher resolution SEM images of each ODS-HEAC have presented in Fig. 11. These images reveal the
265 involvement of multiple wear mechanisms such as oxidation (as indicated by the high oxygen content in
266 Fig. 12 or high-intensity oxide bonds in Fig. 13), abrasion (with ploughing grooves) and adhesion-
267 delamination (with debris and cracks underneath). To explain the latter more, according to the high pin
268 load-low sliding speed, it is possible for localized and minor welding and adhesion to occur as a result of
269 friction welding. This adhesive mechanism is supported by the EDS results depicted in Fig. 12, which
270 show tungsten entering from the pin to the worn surface. The wear mechanisms mentioned commonly
271 occur in high entropy alloys [25]. In Fig. 13, the Raman broad peaks observed at 502 cm^{-1} , 530 cm^{-1} , 626
272 cm^{-1} , 668 cm^{-1} , 1391 cm^{-1} , and 1590 cm^{-1} correspond to Al_2O_3 , Cr_2O_3 , YSZ, Al_2O_3 , Fe_2O_3 , and Cr_2O_3 ,
273 respectively. These results are accordant with findings from other studies [25, 53-57]. These oxide peaks
274 (excluding the one corresponding to YSZ) indicate a higher level of oxidation reaction at the surface of
275 the HEAC samples during sliding. It is evident that samples with higher wear rates (HEA, HEA-
276 5YSZnano, and HEA-10YSZnano) exhibit significant amounts of delamination and oxidation
277 mechanisms. In the case of HEA-5YSZnano, long ploughing grooves demonstrate substantial abrasion
278 wear phenomena. These results demonstrate that, similar to findings in other reference [30], the addition
279 of ceramic particles to HEAs not only enhances hardness, but also reduces wear rates, which are highly
280 desirable outcomes.

281 It should be noted that certain types of defects, such as pores and impurities (e.g., oxide phases), can form
 282 during the mechanical alloying and subsequent SPS processing of metal matrix composites. However,
 283 demonstrating the impact of these defects on the mechanical properties of HEACs poses a challenge and
 284 necessitates more comprehensive investigations, including techniques like atom probe tomography, 3D-
 285 EBSD, and TEM analyses. Nevertheless, in the case of HEA+YSZ composites, the influence of these
 286 defects on mechanical properties can be considered negligible for two primary reasons. First, the analysis
 287 of XRD, EDS, Raman, and SEM results suggests that the proportion of pores and impurities is not
 288 significant. Second, the similarity in pore fraction and impurity percentages across all samples indicates
 289 that these defects have not markedly influenced the mechanical properties.

290 Additionally, the variation in friction coefficient for each sample is presented in Fig. 14. Due to
 291 considerable fluctuations in the CoF results, and to make the curves comparable, the trend line has been
 292 fitted for each graph. In Fig. 14b, the initial wear stage (running-in period) of each sample has been
 293 excluded. It is evident that HEA-10YSZmicro exhibits the lowest coefficient of friction (CoF).
 294 Furthermore, unlike the other samples which display significant CoF fluctuations, HEA-10YSZmicro
 295 demonstrates a steady-state trend, potentially leading to lower friction and dissipation energy. According
 296 to the formula presented in the reference [59], a lower CoF may result in a decrease in temperature rise
 297 and dissipation energy. As a consequence, this can potentially mitigate issues such as deformation,
 298 detachment, and cracking caused by thermal variations. Consequently, as shown in Fig. 10, HEA-
 299 10YSZmicro exhibits the minimum wear width and rate. The desired wear characteristics of HEA-
 300 10YSZmicro become particularly significant when considering the high normal load (30 N)/contact
 301 stresses (more than 2.4 GPa), especially in comparison to experiments conducted in other studies [4, 6]
 302 using lower loads/contact stresses (typically less than 20 N). The stresses are computed using the Hertzian
 303 contact pressure equation (equations 1 and 2) [60], in which F represents the normal load (N) and R
 304 denotes the radius of the pin (mm). Additionally, ν_i and E_i refer to the Poisson's ratio and Young's modulus
 305 of the sample or counterpart (the Poisson's ratio for the samples is regarded as 0.25, while for tungsten
 306 carbide it is 0.3 and the Young's modulus of tungsten carbide is 560 GPa). Therefore, this material emerges
 307 as a promising candidate for use in mechanical components subjected to erosion and wear.

$$308 \text{ Contact stress} = (6F/\pi^3 R^3 E^*)^{1/3} \quad (1)$$

$$309 \frac{1}{E^*} = \frac{1-\nu_1^2}{E_1} + \frac{1-\nu_2^2}{E_2} \quad (2)$$

310

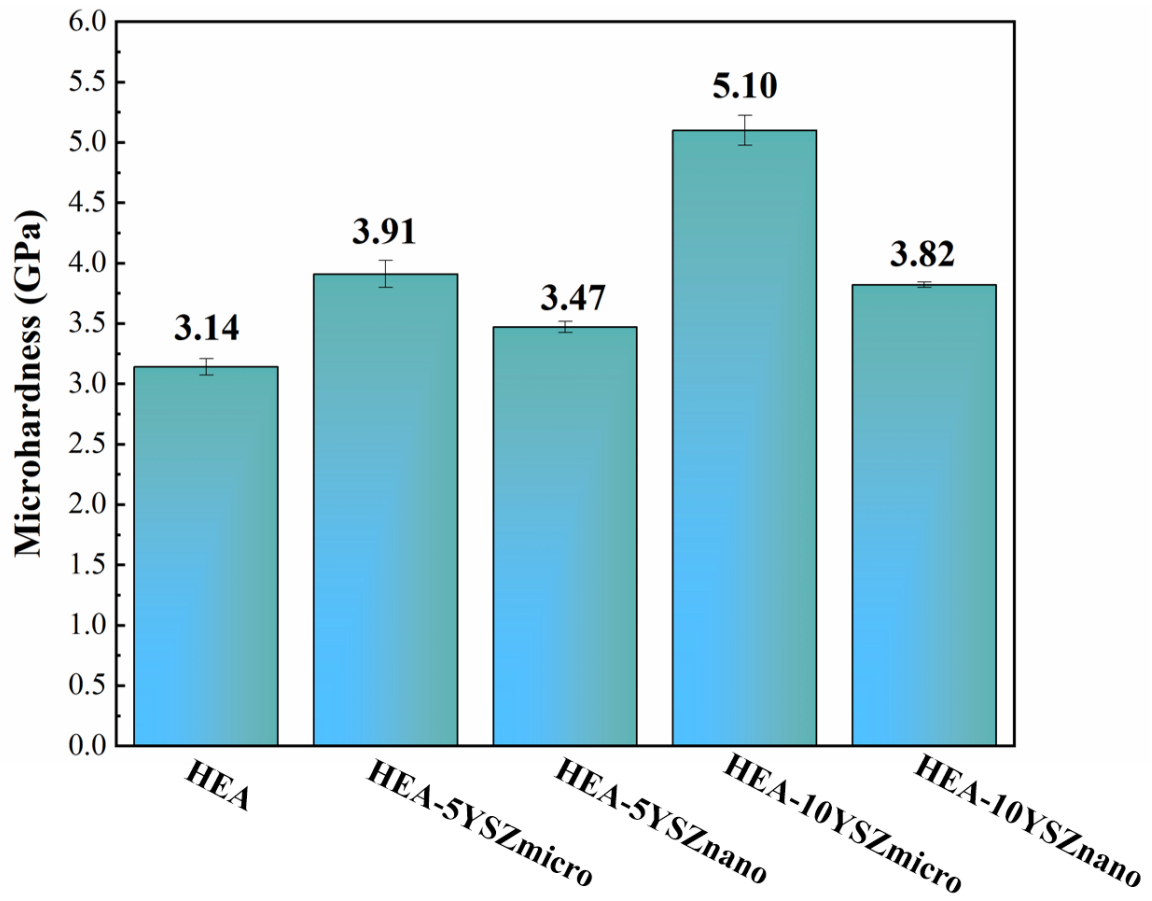


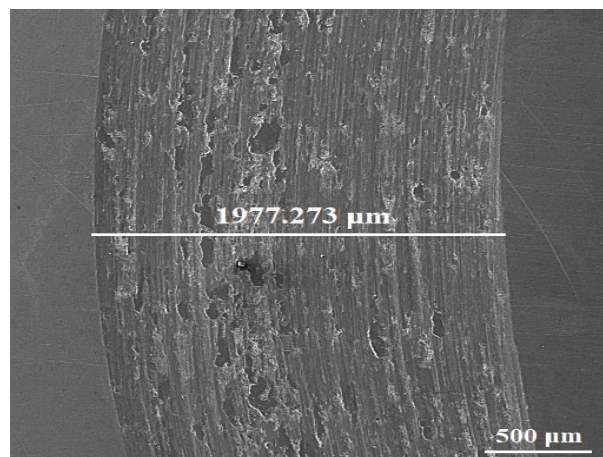
Fig. 8: Micro-hardness results.

311

312

313

314



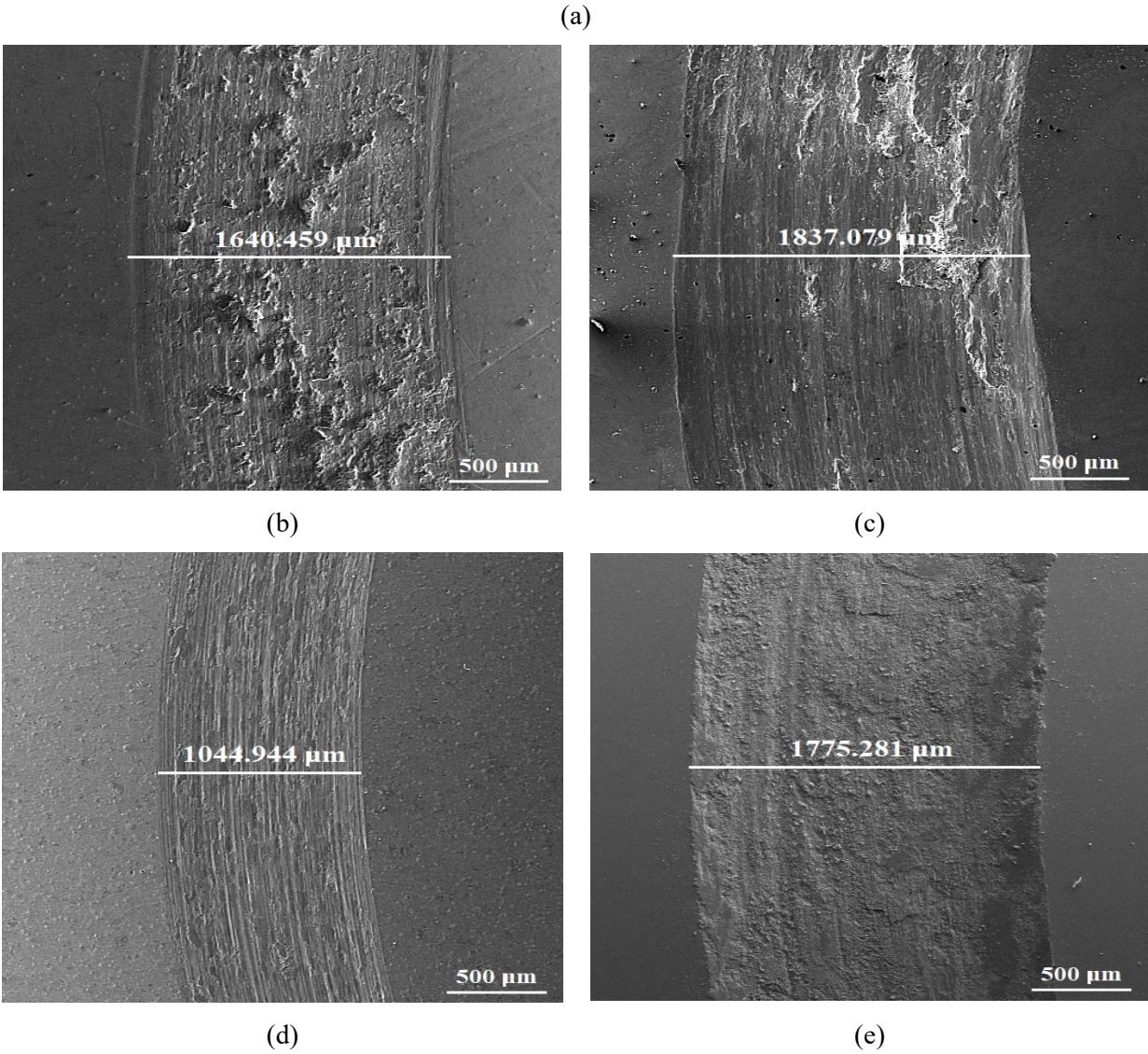
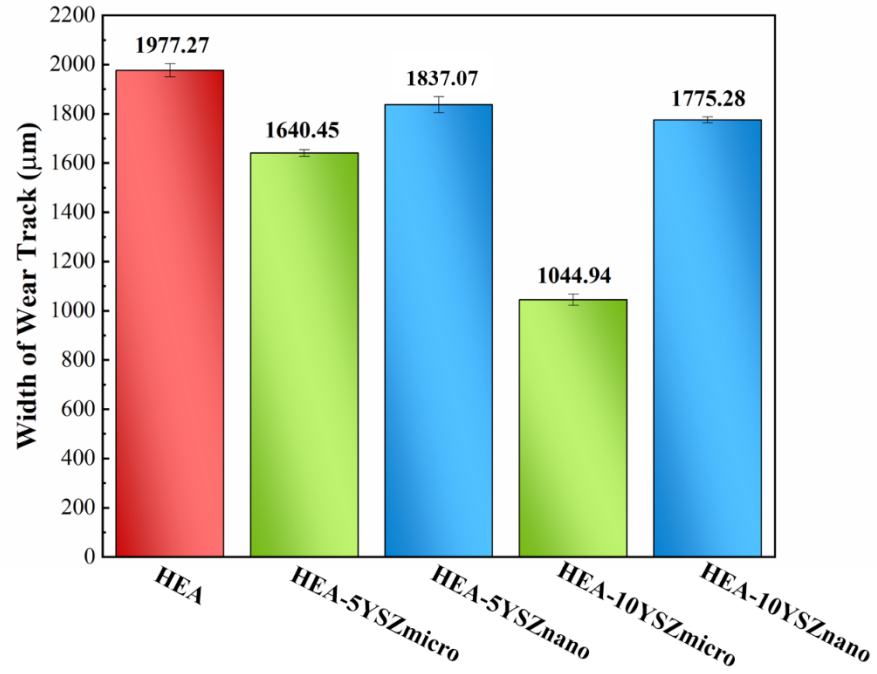
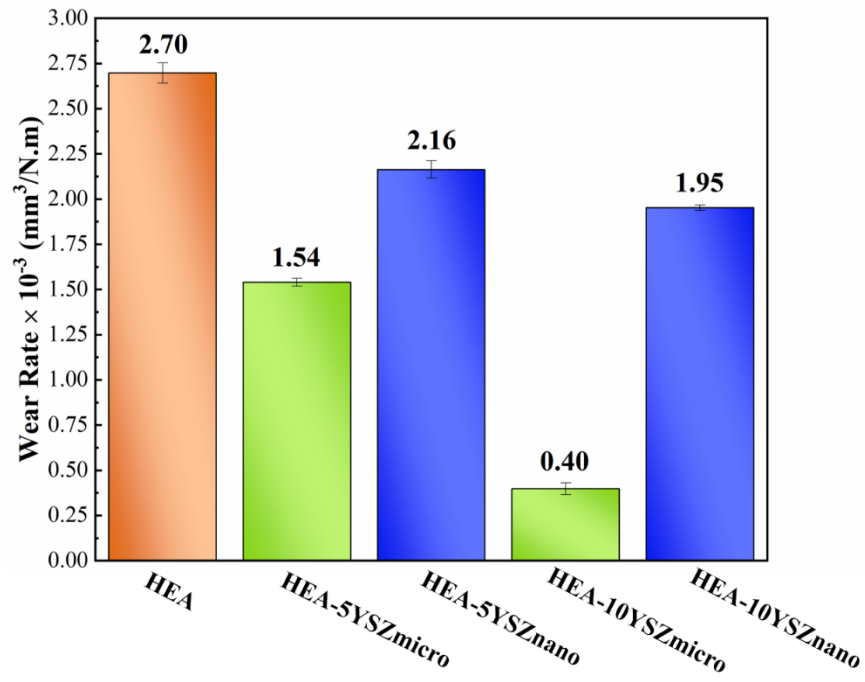


Fig. 9: SEM images related to wear tracks of the composite samples; (a) HEA, (b) HEA-5 wt% YSZmicro, (c) HEA-5 wt% YSZnano, (d) HEA-10 wt% YSZmicro, and (e) HEA-10 wt% YSZnano.

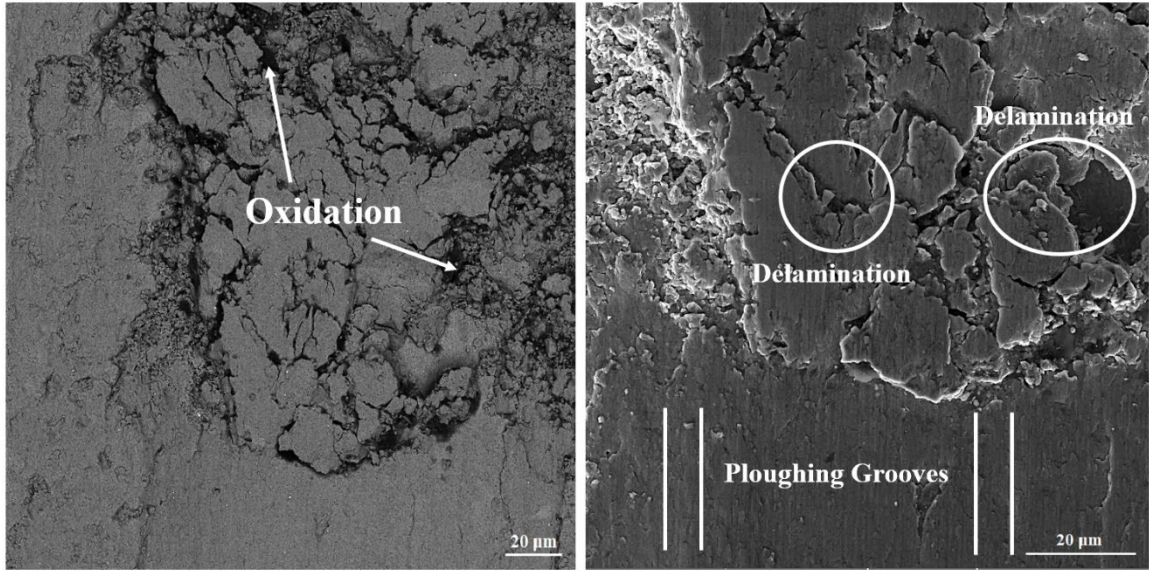


(a)

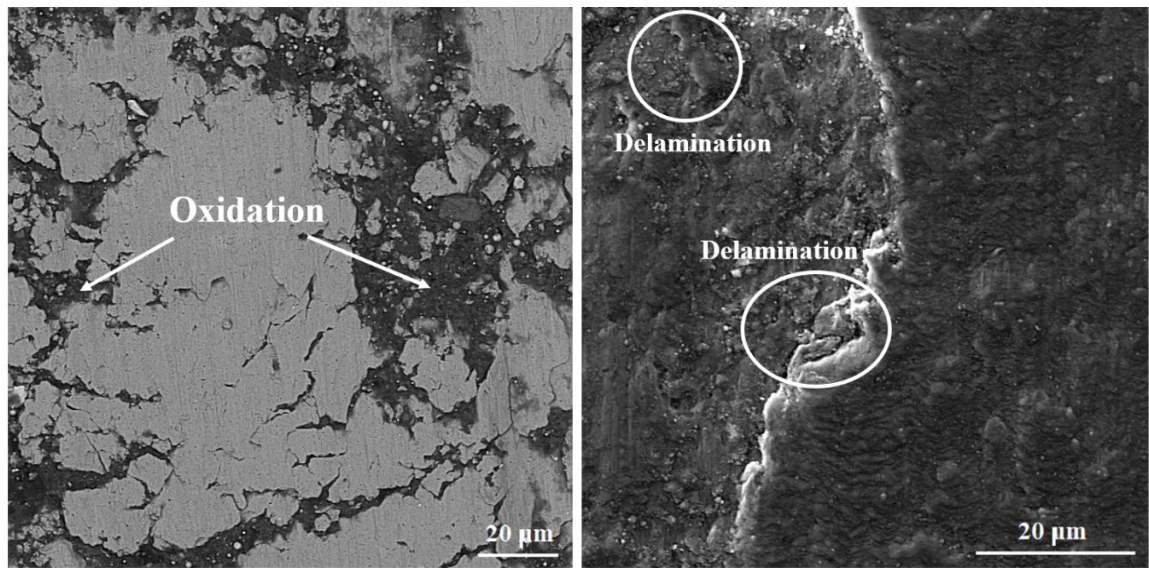


(b)

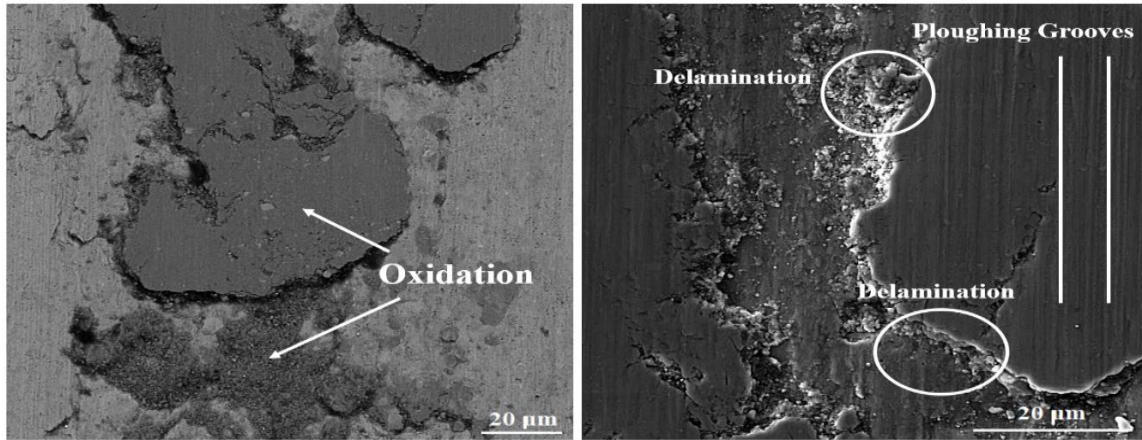
Fig. 10: (a) average wear width and (b) wear rate of samples.



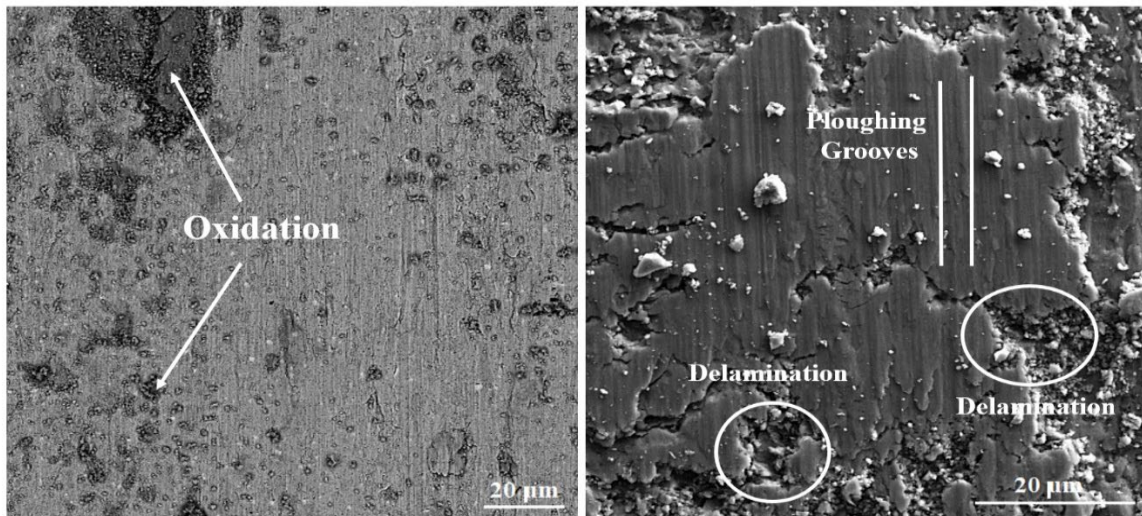
(a)



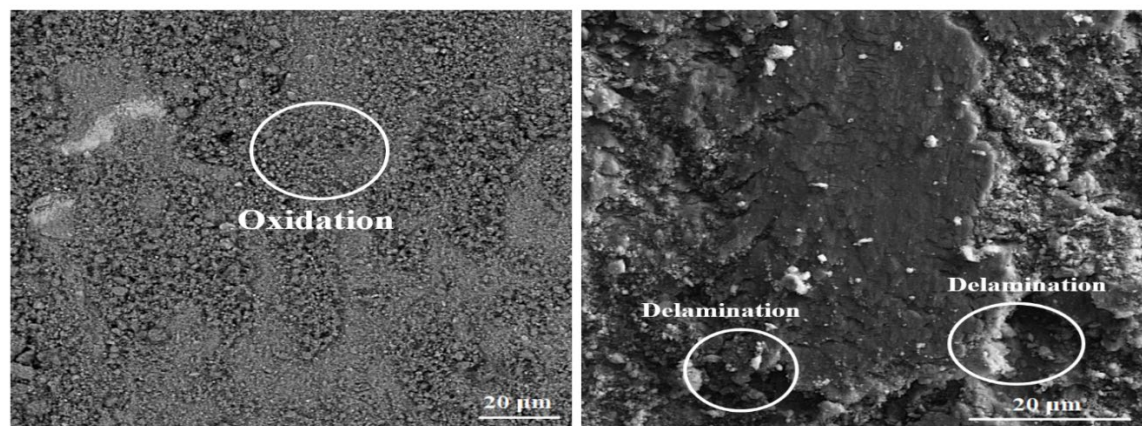
(b)



(c)

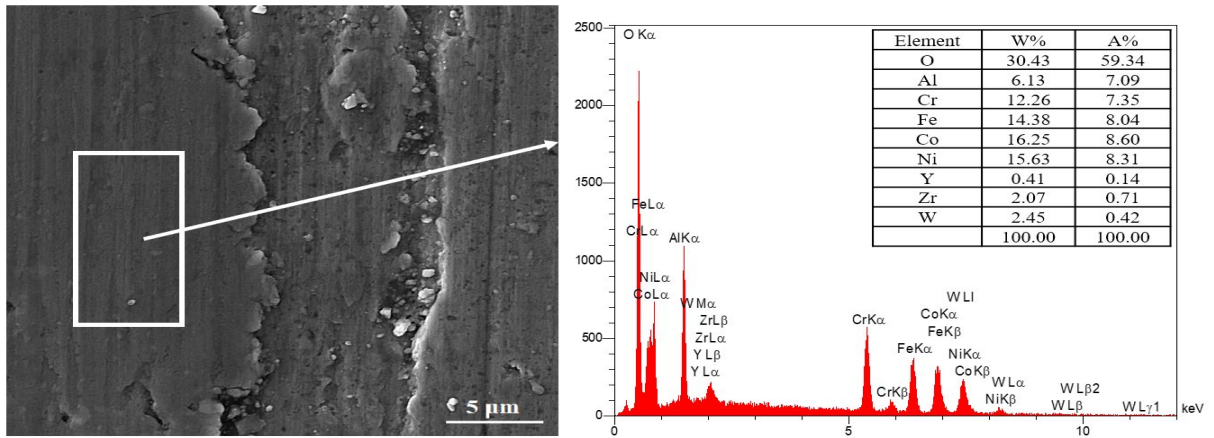


(d)

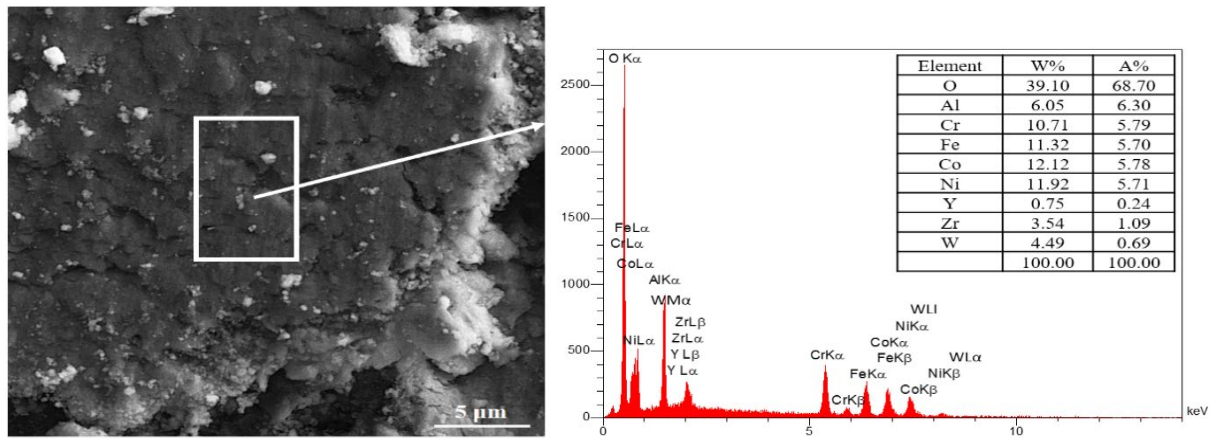


(e)

Fig. 11: SEM micrographs of the worn surfaces of samples; (a) HEA, (b) HEA-5 wt% YSZmicro, (c) HEA-5 wt% YSZnano, (d) HEA-10 wt% YSZmicro, and (e) HEA-10 wt% YSZnano.



(a)



(b)

Fig. 12: EDS analysis of the worn surfaces of samples; (a) HEA-5 wt% YSZnano and (b) HEA-10 wt% YSZnano.

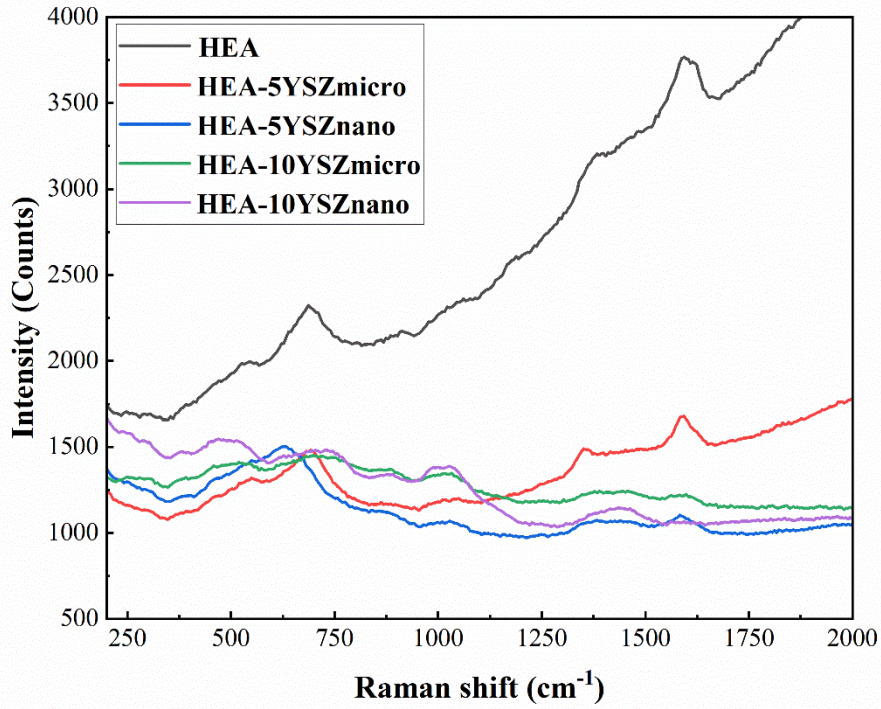
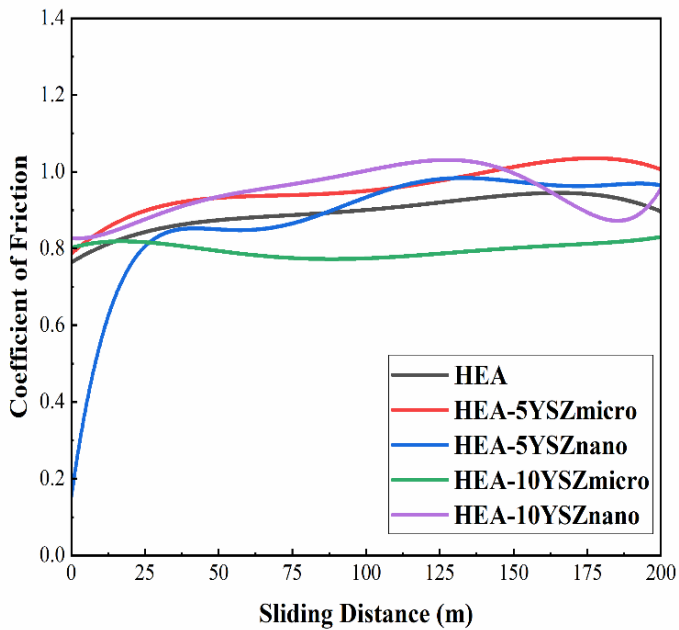
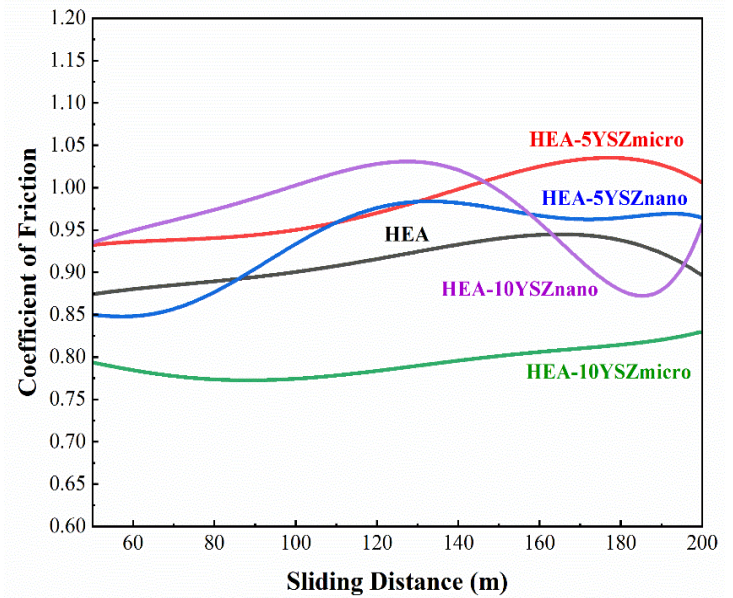


Fig. 13: Raman spectra of worn samples.

319



(a)



(b)

Fig. 14: Fitted curves of CoF for each sample; (a) total variations (b) without running-in period.

320 **4. Conclusions**

321 The microstructure and mechanical properties of AlCoCrFeNi high entropy alloys with varying YSZ size
322 and content have been investigated through a series of tests. The composite phase structure
323 (FCC+BCC+YSZ), as well as hardness and wear behaviors, exhibit significant variation when the size
324 and content of oxide particles are altered. Consequently, it can be inferred that:

- 325 1. Based on the XRD and SEM-EDS results, the level of BCC to FCC ratio is found to be strongly
326 correlated with the YSZ content in ODS-HEAC samples. The ratio of BCC to FCC is higher in
327 micro-sized YSZ samples compared to nano-sized YSZ samples, with the lowest ratio observed in
328 the HEA-10YSZnano sample.
- 329 2. According to the Raman results, it is clear that oxidation can happen during the sintering of
330 powders. Moreover, under sliding conditions, oxide content at the surface can be increased
331 especially in the case of metallic sample (HEA).
- 332 3. At the same oxide particle size, when the YSZ content increases hardness increases and wear rate
333 decreases which is desirable behavior.
- 334 4. At the same oxide particle content, micro-sized YSZ samples show higher hardness and lower
335 wear width. This behavior can be attributed to multiple mechanisms.
- 336 5. Under high load and contact stresses, HEA-10YSZmicro shows steady-state wear and a low
337 friction coefficient (the average is 0.8). Other samples show fluctuations and higher friction
338 coefficients (their average is more than 0.92).

339

340

341

342 **Declaration of Competing Interest**

343 None.

344

345

346

347 **References**

348

- 349 [1] A.O. Mekhrabov, M.V. Akdeniz, Effect of ternary alloying elements addition on atomic ordering
350 characteristics of Fe–Al intermetallics, *Acta Materialia* 47(7), 2067-2075 (1999).
- 351 [2] J.-W. Yeh, S.-K. Chen, S.-J. Lin, J.-Y. Gan, T.-S. Chin, T.-T. Shun, C.-H. Tsau, S.-Y. Chang,
352 Nanostructured High-Entropy Alloys with Multiple Principal Elements: Novel Alloy Design Concepts
353 and Outcomes, *Advanced Engineering Materials* 6(5), 299-303 (2004).
- 354 [3] Z. Li, K.G. Pradeep, Y. Deng, D. Raabe, C.C. Tasan, Metastable high-entropy dual-phase alloys
355 overcome the strength–ductility trade-off, *Nature* 534(7606), 227-230 (2016).
- 356 [4] J. Miao, H. Liang, A. Zhang, J. He, J. Meng, Y. Lu, Tribological behavior of an AlCoCrFeNi_{2.1} eutectic
357 high entropy alloy sliding against different counterfaces, *Tribology International* 153, 106599 (2021).
- 358 [5] Y.A. Alshataif, S. Sivasankaran, F.A. Al-Mufadi, A.S. Alaboodi, H.R. Ammar, Manufacturing
359 Methods, Microstructural and Mechanical Properties Evolutions of High-Entropy Alloys: A Review,
360 *Metals and Materials International* 26(8), 1099-1133 (2020).
- 361 [6] X. Li, Y. Wang, F. Wang, A. Liang, Subsonic-Flame-Sprayed CoCrFeNi, AlCoCrFeNi and
362 MnCoCrFeNi-Based High-Entropy Alloy Coatings and Their Tribological Behaviors, *Journal of Thermal*
363 *Spray Technology* 32(1), 96-110 (2023).
- 364 [7] Y. Wang, R. Wang, J. Lin, L. Wang, Z. Chen, Mechanical and high-temperature wear resistance
365 properties of WC-reinforced AlCoCrFeNiTi_{0.5} high entropy alloy matrix composite, *Ceramics*
366 *International* 50(1, Part B), 2162-2176 (2024).
- 367 [8] K.R. Rao, S.K. Dewangan, A.H. Seikh, S.K. Sinha, B. Ahn, Microstructure and Mechanical
368 Characteristics of AlCoCrFeNi-Based ODS High-Entropy Alloys Consolidated by Vacuum Hot Pressing,
369 *Metals and Materials International* (2023).
- 370 [9] Ł. Rogal, Z. Szklarz, P. Bobrowski, D. Kalita, G. Garzeł, A. Tarasek, M. Kot, M. Szezynger,
371 Microstructure and Mechanical Properties of Al–Co–Cr–Fe–Ni Base High Entropy Alloys Obtained
372 Using Powder Metallurgy, *Metals and Materials International* 25(4) 930-945 (2019).
- 373 [10] J. Feng, Y. Tang, J. Liu, P. Zhang, C. Liu, L. Wang, Bio-high entropy alloys: Progress, challenges,
374 and opportunities, *Frontiers in Bioengineering and Biotechnology* 10 (2022).
- 375 [11] Gao. M.C, Yeh. J.W, Liaw. P.K, Z. Y, High-Entropy Alloys (Fundamentals and Applications),
376 Springer Cham (2016).
- 377 [12] P. Zhou, P.K. Wong, P. Niu, M. Chen, C.T. Kwok, Y. Tang, R. Li, S. Wang, H. Pan, Anodized
378 AlCoCrFeNi high-entropy alloy for alkaline water electrolysis with ultra-high performance, *Science*
379 *China Materials* 66(3), 1033-1041 (2023).
- 380 [13] S.K. Dewangan, A. Mangish, S. Kumar, A. Sharma, B. Ahn, V. Kumar, A review on High-
381 Temperature Applicability: A milestone for high entropy alloys, *Engineering Science and Technology, an*
382 *International Journal* 35, 101211 (2022).
- 383 [14] D.B. Miracle, O.N. Senkov, A critical review of high entropy alloys and related concepts, *Acta*
384 *Materialia* 122, 448-511 (2017).
- 385 [15] Y.F. Ye, Q. Wang, J. Lu, C.T. Liu, Y. Yang, High-entropy alloy: challenges and prospects, *Materials*
386 *Today* 19(6), 349-362 (2016).
- 387 [16] T. Fujieda, H. Shiratori, K. Kuwabara, M. Hirota, T. Kato, K. Yamanaka, Y. Koizumi, A. Chiba, S.
388 Watanabe, CoCrFeNiTi-based high-entropy alloy with superior tensile strength and corrosion resistance
389 achieved by a combination of additive manufacturing using selective electron beam melting and solution
390 treatment, *Materials Letters* 189, 148-151 (2017).

391 [17] J. Fan, W. Zhang, Atomic Scale Diffusion Study in Quaternary and Quinary Alloys of Co–Cr–Fe–
392 Mn–Ni System, *Metals and Materials International* (2023).

393 [18] H. Zheng, R. Chen, G. Qin, X. Li, Y. Su, H. Ding, J. Guo, H. Fu, Microstructure evolution, Cu
394 segregation and tensile properties of CoCrFeNiCu high entropy alloy during directional solidification,
395 *Journal of Materials Science & Technology* 38, 19-27 (2020).

396 [19] H. Yang, J. Li, T. Guo, W.Y. Wang, H. Kou, J. Wang, Fully Recrystallized Al_{0.5}CoCrFeNi High-
397 Entropy Alloy Strengthened by Nanoscale Precipitates, *Metals and Materials International* 25(5), 1145-
398 1150 (2019).

399 [20] A. Shafiei, Design of Eutectic High Entropy Alloys in Al–Co–Cr–Fe–Ni System, *Metals and*
400 *Materials International* 27(1), 127-138 (2021).

401 [21] J.-M. Wu, S.-J. Lin, J.-W. Yeh, S.-K. Chen, Y.-S. Huang, H.-C. Chen, Adhesive wear behavior of
402 Al_xCoCrCuFeNi high-entropy alloys as a function of aluminum content, *Wear* 261(5), 513-519 (2006).

403 [22] C.T. Wang, Y. He, Z. Guo, X. Huang, Y. Chen, H. Zhang, Y. He, Strain Rate Effects on the
404 Mechanical Properties of an AlCoCrFeNi High-Entropy Alloy, *Metals and Materials International* 27(7),
405 2310-2318 (2021).

406 [23] L. Guo, D. Xiao, W. Wu, S. Ni, M. Song, Effect of Fe on microstructure, phase evolution and
407 mechanical properties of (AlCoCrFeNi)_{100-x}Fe_x high entropy alloys processed by spark plasma sintering,
408 *Intermetallics* 103, 1-11 (2018).

409 [24] T.-T. Shun, W.-J. Hung, Effects of Cr Content on Microstructure and Mechanical Properties of
410 AlCoCr_xFeNi High-Entropy Alloy, *Advances in Materials Science and Engineering* 2018, 5826467
411 (2018).

412 [25] Y. Wang, X. Li, A. Liang, Wear behavior and microstructural transformation of single fcc phase
413 AlCoCrFeNi high-entropy alloy at elevated temperatures, *International Journal of Materials Research*
414 113(8), 730-743 (2022).

415 [26] A. Faraji, M. Farvizi, T. Ebadzadeh, H.S. Kim, Microstructure, wear performance, and mechanical
416 properties of spark plasma-sintered AlCoCrFeNi high-entropy alloy after heat treatment, *Intermetallics*
417 149, 107656 (2022).

418 [27] S. Praveen, B.S. Murty, R.S. Kottada, Phase Evolution and Densification Behavior of Nanocrystalline
419 Multicomponent High Entropy Alloys During Spark Plasma Sintering, *JOM* 65(12), 1797-1804 (2013).

420 [28] I. Basu, V. Ocelik, J.T. De Hosson, BCC-FCC interfacial effects on plasticity and strengthening
421 mechanisms in high entropy alloys, *Acta Materialia* 157, 83-95 (2018).

422 [29] M. Farvizi, M. Bahamirian, A. Faraji, H.S. Kim, Role of Particle Size of Al₂O₃ Reinforcement on the
423 Wear Performance of NiTi-Based Composites, *Metals and Materials International* (2023).

424 [30] R. Zhou, G. Chen, B. Liu, J. Wang, L. Han, Y. Liu, Microstructures and wear behaviour of
425 (FeCoCrNi)_{1-x}(WC)_x high entropy alloy composites, *International Journal of Refractory Metals and Hard*
426 *Materials* 75, 56-62 (2018).

427 [31] D. Yim, P. Sathiyamoorthi, S.-J. Hong, H.S. Kim, Fabrication and mechanical properties of TiC
428 reinforced CoCrFeMnNi high-entropy alloy composite by water atomization and spark plasma sintering,
429 *Journal of Alloys and Compounds* 781, 389-396 (2019).

430 [32] B. Li, L. Zhang, Y. Xu, Z. Liu, B. Qian, F. Xuan, Selective laser melting of CoCrFeNiMn high
431 entropy alloy powder modified with nano-TiN particles for additive manufacturing and strength
432 enhancement: Process, particle behavior and effects, *Powder Technology* 360, 509-521 (2020).

433 [33] L. Zong, L. Xu, C. Luo, Z. Jiao, X. Li, W. Sun, S. Wei, Mechanical properties and strengthening
434 mechanism of the nano-sized m-ZrO₂ ceramic particle reinforced NbMoTaW refractory high-entropy
435 alloy, *International Journal of Refractory Metals and Hard Materials* 113, 106201 (2023).

436 [34] S. Yang, X. Yan, K. Yang, Z. Fu, Effect of the addition of nano-Al₂O₃ on the microstructure and
437 mechanical properties of twinned Al_{0.4}FeCrCoNi_{1.2}Ti_{0.3} alloys, *Vacuum* 131, 69-72 (2016).

438 [35] B. Gwalani, R.M. Pohan, O.A. Waseem, T. Alam, S.H. Hong, H.J. Ryu, R. Banerjee, Strengthening
439 of Al_{0.3}CoCrFeMnNi-based ODS high entropy alloys with incremental changes in the concentration of
440 Y₂O₃, *Scripta Materialia* 162, 477-481 (2019).

441 [36] M. Farvizi, T. Ebadzadeh, M.R. Vaezi, E.Y. Yoon, Y.J. Kim, H.S. Kim, A. Simchi, Microstructural
442 characterization of HIP consolidated NiTi–nano Al₂O₃ composites, *Journal of Alloys and Compounds*
443 606, 21-26 (2014).

444 [37] U. Mücke, Ceramic microstructures. Property control by processing. von W. E. Lee und W. M.
445 Rainforth, 590 Seiten, Zahlreiche Abbildungen, Chapman & Hall, London, Glasgow, Weinheim. New
446 York, Tokio, Melbourne, Madras, 1994, £ 89.00, ISBN 0-412-43140-8, *Materials and Corrosion* 47(6),
447 346-347 (1996).

448 [38] M. Woydt, A. Skopp, I. Dörfel, K. Witke, Wear engineering oxides/anti-wear oxides, *Wear* 218(1),
449 84-95 (1998).

450 [39] M. Ghanbariha, M. Farvizi, T. Ebadzadeh, Microstructural development in nanostructured
451 AlCoCrFeNi–ZrO₂ high-entropy alloy composite prepared with mechanical alloying and spark plasma
452 sintering methods, *Materials Research Express* 6(12), 1265b5 (2019).

453 [40] M. Ghanbariha, M. Farvizi, T. Ebadzadeh, A. Alizadeh Samiyan, Effect of ZrO₂ particles on the
454 nanomechanical properties and wear behavior of AlCoCrFeNi–ZrO₂ high entropy alloy composites, *Wear*
455 484-485, 204032 (2021).

456 [41] T. Liao, Y.-K. Cao, W.-M. Guo, Q.-H. Fang, J. Li, B. Liu, Microstructure and mechanical property
457 of NbTaTiV refractory high-entropy alloy with different Y₂O₃ contents, *Rare Metals* 41(10), 3504-3514
458 (2022).

459 [42] A. Sanaty-Zadeh, Comparison between current models for the strength of particulate-reinforced metal
460 matrix nanocomposites with emphasis on consideration of Hall–Petch effect, *Materials Science and*
461 *Engineering: A* 531, 112-118 (2012).

462 [43] Z. Zhang, Y.H. Xie, X.Y. Huo, S.L.I. Chan, J.M. Liang, Y.F. Luo, D.K.Q. Mu, J. Ju, J. Sun, J. Wang,
463 Microstructure and mechanical properties of ultrafine grained CoCrFeNi and CoCrFeNiAl_{0.3} high entropy
464 alloys reinforced with Cr₂O₃/Al₂O₃ nanoparticles, *Materials Science and Engineering: A* 816, 141313
465 (2021).

466 [44] F.S. Kaplan, I.G. Shulik, L.S. Alekseenko, G.P. Orekhova, Properties of slips of zirconia stabilized
467 by oxides of rare earth metals, *Refractories* 36(3), 82-85 (1995).

468 [45] O.A. Graeve, Zirconia, in *Ceramic and Glass Materials: Structure, Properties and Processing*, J.F.
469 Shackelford and R.H. Doremus, Editors. Springer US: Boston, MA. p. 169-197 (2008).

470 [46] G.P. Cousland, X.Y. Cui, A.E. Smith, A.P.J. Stampfl, C.M. Stampfl, Mechanical properties of
471 zirconia, doped and undoped yttria-stabilized cubic zirconia from first-principles, *Journal of Physics and*
472 *Chemistry of Solids* 122, 51-71 (2018).

473 [47] S.A. Ataie, R. Keshtmand, M.R. Zamani-Meymian, Nano-mechanical properties of Cr-Zr-Nb-N
474 medium entropy alloy films produced by reactive sputtering, *International Journal of Refractory Metals*
475 *and Hard Materials* 110, 106006 (2023).

476 [48] S.A. Ataie, M. Soltanieh, R. Naghizadeh, A. Cavaleiro, M. Evaristo, F. Fernandes, F. Ferreira, Effect
477 of substrate bias voltage on structural and tribological properties of W-Ti-C-N thin films produced by
478 combinational HiPIMS and DCMS co-sputtering, *Wear* 520-521, 204654 (2023).

479 [49] R. Liu, D.Y. Li, Y.S. Xie, R. Llewellyn, H.M. Hawthorne, Indentation behavior of pseudoelastic TiNi
480 alloy, *Scripta Materialia* 41(7), 691-696 (1999).

481 [50] K. Raja, P. Ganeshan, B.K. Singh, R.K. Upadhyay, P. Ramshankar, V. Mohanavel, Effect of mol.%
482 of Yttria in Zirconia matrix alongside a comparative study among YSZ, alumina & ZTA ceramics in terms
483 of mechanical and functional properties, *Sādhanā* 48(2), 72 (2023).

- 484 [51] G. Fiquet, C. Narayana, C. Bellin, A. Shukla, I. Estève, A.L. Ruoff, G. Garbarino, M. Mezouar,
485 Structural phase transitions in aluminium above 320GPa, *Comptes Rendus Geoscience* 351(2), 243-252
486 (2019).
- 487 [52] S.A. Makhlof, E. Ivanov, K. Sumiyama, K. Suzuki, Structural and magnetic properties of
488 nanocrystalline b.c.c. cobalt particles obtained by leaching of mechanically alloyed Co Al, *Journal of*
489 *Alloys and Compounds* 189(1), 117-121 (1992).
- 490 [53] S. Tailor, M. Singh, A.V. Doub, Synthesis and Characterization of Yttria-Stabilized Zirconia (YSZ)
491 Nano-Clusters for Thermal Barrier Coatings (TBCs) Applications, *Journal of Cluster Science* 27(4), 1097-
492 1107 (2016).
- 493 [54] B.P. Dhonge, T. Mathews, S. Rajagopalan, S. Dash, S. Dhara, A.K. Tyagi, Cubic fluorite yttria
494 stabilized zirconia (YSZ) film synthesis by combustion chemical vapour deposition(C-CVD),
495 *International Conference on Nanoscience, Engineering and Technology (ICONSET 2011)*, 2011, pp. 65-
496 68.
- 497 [55] J. Yang, W.N. Martens, R.L. Frost, Transition of chromium oxyhydroxide nanomaterials to
498 chromium oxide: a hot-stage Raman spectroscopic study, *Journal of Raman Spectroscopy* 42(5), 1142-
499 1146 (2011).
- 500 [56] K. Song, Y. Lee, M.R. Jo, K.M. Nam, Y.-M. Kang, Comprehensive design of carbon-encapsulated
501 Fe₃O₄ nanocrystals and their lithium storage properties, *Nanotechnology* 23(50), 505401 (2012).
- 502 [57] S. Benafia, D. Reirant, S. Yapi Brou, B. Panicaud, J.L. Grosseau Poussard, Influence of Surface
503 Mechanical Attrition Treatment on the oxidation behaviour of 316L stainless steel, *Corrosion Science*
504 136, 188-200 (2018).
- 505 [58] C. Laurent, A. Rousset, Metal-Oxide Ceramic Matrix Nanocomposites, *Key Engineering Materials*
506 108-110, 405-406 (1995).
- 507 [59] M. Bai, L. Yang, J. Li, L. Luo, S. Sun, B. Inkson, Mechanical and tribological properties of Si and
508 W doped diamond like carbon (DLC) under dry reciprocating sliding conditions, *Wear* 484-485, 204046
509 (2021).
- 510 [60] X. Liu, Y. Wang, L. Qin, Z. Guo, Z. Lu, X. Zhao, H. Dong, Q. Xiao, Friction and wear properties of
511 a novel interface of ordered microporous Ni-based coating combined with MoS₂ under complex working
512 conditions, *Tribology International* 189, 108970 (2023).

513